

Optical control of spin-splitting in an altermagnet

Sangeeta Rajpurohit,^{1,*} Revsen Karaalp,² Yuan Ping,^{3,4,5} L.Z. Tan,¹ Tadashi Ogitsu,⁶ and Peter E. Blöchl^{7,8}

¹*Molecular Foundry, Lawrence Berkeley National Laboratory, USA*

²*Advanced Light Source, Lawrence Berkeley National Laboratory, USA*

³*Department of Materials Science and Engineering,*

University of Wisconsin-Madison, Madison, Wisconsin 53706, United States

⁴*Department of Physics, University of Wisconsin-Madison, Madison, Wisconsin 53706, United States*

⁵*Department of Chemistry, University of Wisconsin-Madison, Madison, Wisconsin 53706, United States*

⁶*Lawrence Livermore National Laboratory, Livermore, USA*

⁷*Institute for Theoretical Physics, Clausthal University of Technology, Germany*

⁸*Institute for Theoretical Physics, Georg-August-Universität Göttingen, Germany*

(Dated: September 27, 2024)

Manipulating and controlling the band structure and the spin-splitting in the newly discovered class of magnetic materials known as 'altermagnets' is highly desirable for their application in spintronics. Based on real-time simulations for an interacting multiband tight-binding model, we propose optical excitations as an effective way to selectively control the spin-splitting of an altermagnet. The consistent treatment of electronic interactions and electron-phonon coupling in the model allows for a systematic study of the effect of these interactions on the spin-splitting of the altermagnet in the ground as well as in the excited-state. Our simulations reveal that optical excitations modify the band structure and thus lead to significant changes in the spin-splitting within 50 fs. The relative spin-splitting in the conduction band grows up to four times in the optically excited altermagnet. We disentangle the roles of Coulomb U and J in the enhancement of the spin-splitting in the photoexcited state. Our study elucidates the potential for exploiting optical control of spin-splitting gaps to obtain desirable properties in altermagnets on the fastest possible timescales.

Altermagnetism, which has emerged as a new class of magnetism besides ferromagnetism and antiferromagnetism, has drawn a lot of attention in condensed matter physics [1–3]. Altermagnets exhibit properties of both ferromagnets (FMs) and antiferromagnets (AFMs). Similarly to AFMs, they have zero net magnetization with local magnetic moments alternating in real space. However, like FMs, they break Kramers's degeneracy in reciprocal space in the absence of spin-orbit coupling (SOC). Instead of spatial translation and spin-inversion, the opposite spin sublattices in an altermagnet are connected by spatial rotation. Due to the breaking of time-reversal symmetry in momentum space, there are several unconventional anomalous magnetic responses predicted in altermagnets, such as the anomalous Hall effect [2, 4, 5] and the magneto-optical Kerr effect [6], which have been verified by experiments.

The spin-splitting in altermagnets originates from anisotropic exchange interactions. Many materials with the potential to host altermagnetism have been identified [1, 7]. However, the predicted spin-splitting of most of them is less than 0.50 eV. Few exceptions are RuO₂, CrSb and MnTe. The maximum spin-splitting of 1.4 eV is predicted for RuO₂, followed by CrSb and MnTe with spin-splittings of 1.2 eV and 1.1 eV, respectively [1].

After the discovery of alternative magnetism, most research efforts have focused on identifying promising materials. Although spin-splitting plays a pivotal role in most of the predicted applications of altermagnet, in-

cluding spintronics, the possible ways to manipulate and control the spin-splitting gap in these materials remain largely unexplored. Advances in ultrafast science have resulted in promising routes to manipulate and control the properties of materials [8–10]. Optical tuning of spin-splitting gaps can offer exciting opportunities to modify the altermagnetic properties on ultrafast timescales.

In this study, we demonstrate the realization of altermagnetism with spin-splitting of d-wave symmetry in the presence of orbital ordering using a multiband interacting tight-binding (TB) model. Our study shows that spin-splitting in the altermagnetic ground state strongly depends on Coulomb U , but remains relatively unaffected by Coulomb exchange J . Coulomb J only affects the local magnetic moment. The dependence of spin-splitting gaps on Coulomb parameters suggests that these can be manipulated in the altermagnetic state on ultrafast timescales via intense photoexcitation. Our real-time simulations based on the TB-model reveal significant changes in the band structure and spin-splitting of the altermagnet induced following the optical excitation. Notably, the simulations predict substantial alterations in spin-splitting in the conduction band, which develop fully within 75 fs. Furthermore, increasing the light-pulse intensity further amplifies the spin-splitting. Our findings demonstrate that optical excitations offer an effective approach to modify spin-splitting in altermagnets with correlated electrons.

Firstly, we construct a 2D interacting TB-model that describes the generic features of altermagnetism driven by orbital ordering in strongly correlated oxides. We start with a square planar lattice of corner-sharing oxy-

* srajpurohit@lbl.gov

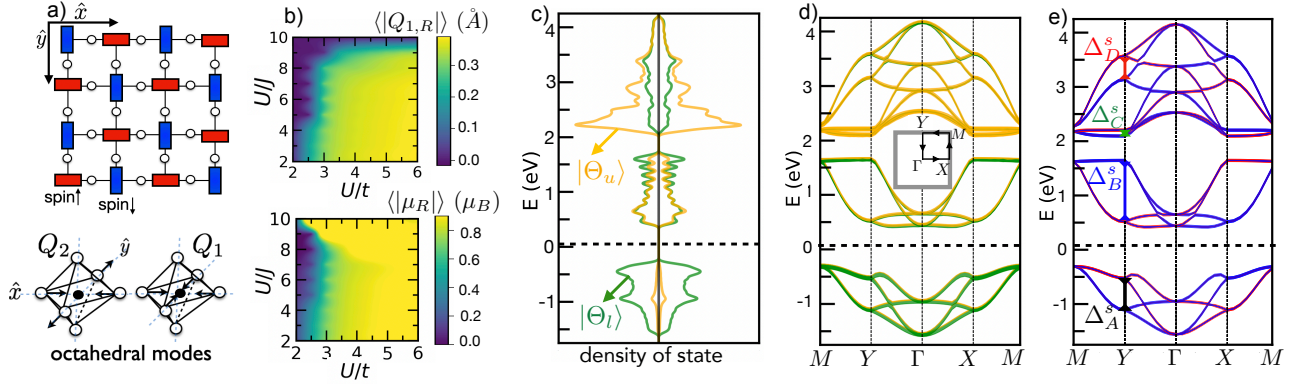


FIG. 1. Altermagnetic ground state of the TB model described in the text before photoexcitation. (a) Spin and orbital order hosting altermagnetism: The rectangles describe the spin and orbital polarization of the TM sites. Blue and red specify the two opposite spin orientations directions. The orientation, horizontal vs. vertical, encodes the orbital polarization of the e_g -electron in the xy -plane along the x and y directions, respectively. (b) Average local magnetic moment $\langle |\mu_R| \rangle$ (bottom) and octahedral modes $\langle |Q_{2,R}| \rangle$ (top) in the $U/J - U/t$ plane. (c-d) Density of states (DOS) (c) and band structure (d) projected on local orbitals $|\Theta_l\rangle$ (green) and $|\Theta_u\rangle$ (orange). The left and right DOS shows spin-up and spin-down contributions. The thickness of the color represents the intensity of each component in the band structure. (e) Band structure of the altermagnetic state projected onto spin-up (blue) and spin-down (red) components, with the thickness of the colors representing the intensity of each component. The band structures are plotted along high symmetry points $M(\pi, \pi) - Y(0, \pi) - \Gamma(0, 0) - X(\pi, 0) - M(\pi, \pi)$. The plots in (b) use $U=2.50$ eV. The plots c-e use $t = 0.833$ eV, $U/t = 3.0$ and $U/J = 7.0$.

gen octahedra. Each such oxygen octahedron hosts a transition-metal (TM) ion in its center. For each TM site R we consider the d -orbitals of e_g symmetry, $d_{x^2-y^2}$ and $d_{3z^2-r^2}$ and two octahedral distortion modes.

The potential energy $E_{pot}[\{\psi_{\sigma,\alpha,R,n}\}, \{Q_{i,R}\}]$ of the proposed interacting TB-model is expressed in terms of one-electron wave functions $|\psi_n\rangle = \sum_{\sigma,\alpha,R} |\chi_{\sigma,\alpha,R}\rangle \psi_{\sigma,\alpha,R,n}$ and octahedral distortion modes $Q_{i,R}$. The basis set $|\chi_{\sigma,\alpha,R}\rangle$ for consists of local spin orbitals with spin $\sigma \in \{\uparrow, \downarrow\}$ and orbital character $\alpha \in \{d_{x^2-y^2}, d_{3z^2-r^2}\}$.

The potential energy

$$E_{pot} = E_e + E_{ph} + E_{e-ph} \quad (1)$$

consists of the energy E_e of the electronic subsystem, the energy E_{ph} the phonon subsystems and the electron-phonon (el-ph) interaction energy E_{e-ph} .

Electronic subsystem: The electronic energy $E_e = E_{hop} + E_{coul}$ consists of the kinetic energy E_{hop} and the Coulomb interaction E_{coul} . The kinetic energy is expressed as

$$E_{hop} = \sum_{R,R',\sigma,n} f_n \sum_{\alpha,\alpha'} \psi_{\sigma,\alpha,R,n} T_{\alpha,\alpha',R,R'} \psi_{\sigma,\alpha',R,n}^* \quad (2)$$

where the hopping-matrix elements $T_{\alpha,\alpha',R,R'}$ contribute only onsite and nearest-neighbor terms between the TM-sites. The f_n are the occupations of the one-particle wave functions $|\psi_n\rangle$. The hopping matrix elements along x and y directions are defined as

$$T_{R,R'}^x = -\frac{1}{4} t_{hop} \begin{pmatrix} 3 & -\sqrt{3} \\ -\sqrt{3} & 1 \end{pmatrix} \quad (3)$$

$$T_{R,R'}^y = -\frac{1}{4} t_{hop} \begin{pmatrix} 3 & +\sqrt{3} \\ +\sqrt{3} & 1 \end{pmatrix} \quad (4)$$

The Coulomb interaction E_{coul}

$$\begin{aligned} E_{coul} &= \frac{1}{2} (U - 3J_{xc}) \sum_R \left(\sum_{\sigma,\alpha} \rho_{\sigma,\alpha,\sigma,\alpha,R} \right)^2 \\ &\quad - \frac{1}{2} (U - 3J_{xc}) \sum_R \sum_{\sigma,\alpha,\sigma',\beta} |\rho_{\sigma,\alpha,\sigma',\beta,R}|^2 \\ &\quad + \frac{1}{2} J_{xc} \sum_R \sum_{\sigma,\sigma'} (-1)^{\sigma-\sigma'} \sum_{k \in \{x,z\}} \\ &\quad \times \left[\left(\sum_{\alpha,\beta} \rho_{\sigma,\alpha,\sigma',\beta,R} \sigma_{\beta\alpha}^{(k)} \right) \left(\sum_{\alpha,\beta} \rho_{-\sigma,\alpha,-\sigma',\beta,R} \sigma_{\beta\alpha}^{(k)} \right) \right. \\ &\quad \left. + \left(\sum_{\alpha} \rho_{\sigma,\alpha,\sigma',\alpha,R} \right) \left(\sum_{\alpha} \rho_{-\sigma,\alpha,-\sigma',\alpha,R} \right) \right], \quad (5) \end{aligned}$$

is conveniently expressed in terms of the on-site terms of the one-particle-reduced density matrix $\hat{\rho}$ with the matrix elements defined as

$$\rho_{\sigma,\alpha,R,\sigma',\alpha',R} = \sum_n f_n \psi_{\sigma,\alpha,R,n} \psi_{\sigma',\alpha',R,n}^* \quad (6)$$

Phononic subsystem: The phononic subsystem consists of two octahedral modes of oxygen around every TM-site R : a Jahn-Teller (JT) mode $Q_{2,R}$ and a breathing mode $Q_{1,R}$ [11]. These phonon modes are defined by the displacement vectors of oxygen ions from their equilibrium positions. The JT mode is an asymmetric expansion of an octahedron in the plane, i.e. expansion along x and contraction along the y -direction. The breathing mode is the isotropic expansion of the oxygen octahedron.

The restoring energy of this phononic sub-system

E_{e-ph} is expressed as

$$E_{ph} = \sum_R \left(\frac{1}{2} k_{JT} Q_{2,R}^2 + \frac{1}{2} k_{br} Q_{1,R}^2 \right) \quad (7)$$

where K_{JT} and K_{br} are the restoring force constants of the JT and breathing mode. Due to the shared oxygen ions, the octahedral distortions are highly cooperative.

Electron-phonon coupling: We consider strong coupling between the eg-electron at TM-sites to the local modes $Q_{1,R}$ and $Q_{2,R}$ [11] (see SI). In 3d TM oxides like manganites and nickelates, this type of el-ph interaction is another mechanism besides the Coulomb interaction, which causes long-range orbital ordering [10, 12, 13]. The el-ph coupling E_{el-ph} in the model is defined as

$$E_{e-ph} = \sum_{R,\sigma} \sum_{\alpha,\beta} \rho_{\sigma,\alpha,\beta,R} M_{\beta,\alpha}^Q(Q_{1,R}, Q_{2,R}). \quad (8)$$

Here g_{JT} and g_{br} are the el-ph coupling constants and $M^Q(Q_{1,R}, Q_{2,R})$ is defined as

$$M^Q(Q_{1,R}, Q_{2,R}) = \begin{pmatrix} -g_{br} Q_{1,R} & g_{JT} Q_{2,R} \\ g_{JT} Q_{2,R} & -g_{br} Q_{1,R} \end{pmatrix} \quad (9)$$

The TB-model can describe the strong inequivalent local crystal environment caused by local el-ph coupling and electronic interactions for two sublattices with opposite spins, which reduces the symmetry as needed for alternating spin-splitting of the energy bands in reciprocal space.

We take model parameters from our previous study as a reference [10, 11, 14]. The reference model parameters are $g_{br} = 2.988$ eV/Å, $K_{br} = 10.346$ eV/Å², $g_{JT} = 2.113$ eV/Å, $K_{JT} = 5.173$ eV/Å², $U/t = 4.29$, $U/J = 2.63$ and $t_{hop} = t = 0.585$ eV. In the present study, we are interested in the effect of electronic interactions and correlations on the altermagnetic properties, we vary U , J and t_{hop} while keeping the other parameters fixed.

Altermagnetic ground-state: We investigate the region of phase diagram with the altermagnetic ground-state, shown in Figure 1-a. We consider one electron per TM-site. Figures 1-b displays the changes in the average local mode $\langle Q_{1,R} \rangle$ and the magnetic moment $\langle |m_R| \rangle$ at the TM-sites in the altermagnetic ground-state as a function of U/t and U/J for $U=2.50$ eV. For $U/J < 2.5$ and $U/t < 2.0$, the system exhibits a non-magnetic metallic phase characterized by TM-sites with zero magnetic and orbital moment. As U/J and U/t increase, the system undergoes metallic to an insulating altermagnetic phase transition. In the altermagnetic phase, the TM-sites have finite magnetic moments and eg-orbital polarization. These local magnetic moments are arranged in antiferromagnetic (AFM) order. The local eg-orbital polarization forms long range staggered orbital ordering as shown in Figure 1-a. This altermagnetic state remains stable for $2.5 < U/J < 6.0$ and $2.0 < U/t < 6.0$.

Figures 1-c show the density of states of the altermagnetic ground-state. In the ground state, all TM-sites have

one eg-electron and are JT active. The JT-effect lifts the degeneracy of the local eg-orbitals. The lower filled eg-state $|\Theta_{l,R}\rangle$ located between -1.5 and 0 eV is described by the linear combination

$$|\Theta_{l,R}\rangle = -\sin(\gamma)|d_{x^2-y^2}\rangle \pm \cos(\gamma)|d_{3z^2-r^2}\rangle \quad (10)$$

of the eg-orbitals $d_{x^2-y^2}$ and $d_{3z^2-r^2}$ at site R with $\gamma=60^\circ$. The corresponding unoccupied state $|\Theta_{u,R}\rangle$ are

$$|\Theta_{u,R}\rangle = \cos(\gamma)|d_{x^2-y^2}\rangle \pm \sin(\gamma)|d_{3z^2-r^2}\rangle. \quad (11)$$

The upper sign in front of the $|d_{3z^2-r^2}\rangle$ -state describes an orbital polarization along x and the lower sign describes an orbital polarization along the y direction.

Figure 1-e shows the spin-polarized band structure of the calculated altermagnet state. Clearly, the spin degeneracy of the bands is lifted in momentum space, with the largest spin-splitting gap at high-symmetry points $X=(\pi, 0)$ and $Y=(0, \pi)$. The spin-splitting is present for both the valence band and the conduction band. The magnitude of the spin-splitting for the valence band, indicated by Δ_A^s in Figure 1-e (black) is approximately 0.57 eV. The spin-splitting of 1.10 eV in the lower conduction band, indicated by Δ_B^s (blue), is significantly higher than the corresponding values of $\Delta_C^s = 0.07$ eV (green) and $\Delta_D^s = 0.45$ eV (red) in the upper conduction band. The spin-polarized bands with opposite spins are related by $\pi/2$ rotations in the momentum space.

Figure 2 shows the magnitude of the spin-splitting gap as a function of U/t and U/J . The spin-splitting gap Δ_A^s of the valence band and Δ_B^s of the lower conduction band decreases with U/t . The spin-splitting in the upper conduction band Δ_D^s increases with U/t , while Δ_C^s decreases with U/t . The spin-splitting gaps remain largely unaffected, while the magnetic moments are weakly affected by U/J .

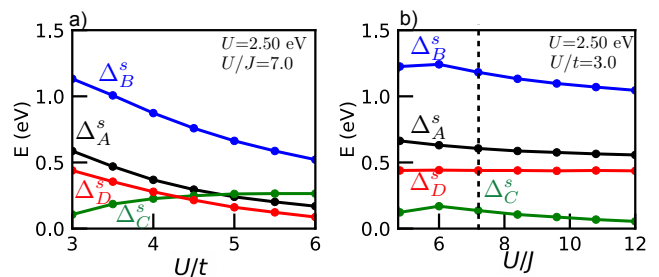


FIG. 2. Spin-splitting gaps in the altermagnetic ground state as functions of U/t (a) and U/J (b). The color codes are the same as 1-e. The other model parameters are set to reference values, which are specified in the main text. The vertical dashed line in (b) indicates $U/J=7.0$ used to study photoexcitation.

The above study of the phase diagram suggests that the properties of the altermagnetic state in correlated electrons systems are sensitive to the Coulomb U and J parameters. The strength of electronic interactions and correlations can be altered through material composition

or external means, such as applying an electromagnetic field or varying the temperature. In the following sections, we use real-time simulations based on the proposed TB-model to demonstrate optical excitations as an effective way to modify the properties of altermagnet on ultrafast timescales.

Photo-excitation study with rt-TDDFT: To study the evolution of spin-splitting under photo-excitation in the altermagnetic state described above, we employ a simulation framework similar to real-time time-dependent density-functional theory (rt-TDDFT) formalism [15] based on the model defined in Eq.1. The one-particle wavefunctions of eg-electrons are propagated according to the time-dependent Schrödinger equation. For the sake of simplicity, the atoms are kept frozen while studying the photoexcitation. The photoexcitation is described by an explicit time-dependent vector potentials $\vec{A}(t) = \vec{e}_s \omega \text{Im}(A_o e^{-i\omega t}) g(t)$ which is coupled to the electrons using Peierls substitution method [16]. Here, A_o is the amplitude of the vector potential and ω is angular frequency. The envelope $g(t)$ of the light pulse is a Gaussian with a width of 30 fs. The polarization \vec{e}_s of light is along the $\hat{x} + \hat{y}$ or the $\hat{x} - \hat{y}$ direction. The unit cell consists of $N=4$ TM-sites and 8 oxygen atoms. The simulations are performed with periodic boundary conditions on a 24×24 k-point grid.

Absorption Spectra: The optical absorption of the altermagnetic state as a function of photon energy $\hbar\omega$ is shown in the inset of Figure 3-a. It is expressed in terms of the photon-absorption density D_p , i.e. the total number of photons absorbed per site. The photon-absorption density is computed from energy difference before and after the light pulse as $D_p = \delta E_{pot} / \hbar\omega N$ with E_{pot} from Eq. 1. We attribute the broad absorption peak around $\hbar\omega_p = 2.39$ eV to dipole-allowed inter-site electronic transitions from majority to minority spin orbitals located on nearest-neighbor TM-sites belonging to opposite spin sublattices.

Spin-splitting in the photo-excited state: Let us examine the changes of the spin-splitting gaps upon optical excitation of the altermagnet. We select the photon energy $\hbar\omega_p = 2.39$ eV with the maximum optical absorption.

For the discussion ahead, we discriminate between two sets of time-dependent wave functions. One set of one-particle wave functions with symbol $|\psi_n(\vec{k}, t)\rangle$ defines the time-dependent Slater determinant. These wave functions are obtained via the *time-dependent* Schrödinger equation with the Hamiltonian $\hat{h}(\vec{k}, t)$. The second set of one-particle wave functions with symbol $|\phi_n(\vec{k}, t)\rangle$ is obtained with the same instantaneous Hamiltonian $\hat{h}(\vec{k}, t)$, but using the *time-independent* Schrödinger equation. The eigenvalues of this Hamiltonian are used to calculate the band structure and spin-splitting gaps Δ^s . The instantaneous occupations $f_m(\vec{k}, t)$ of the eigenstates of the Hamiltonian are obtained by projecting the time-dependent wave functions $|\psi_n(\vec{k}, t)\rangle$ onto the eigenstates $|\phi_m(\vec{k}, t)\rangle$ of the Hamiltonian, i.e. $f_m(\vec{k}, t) =$

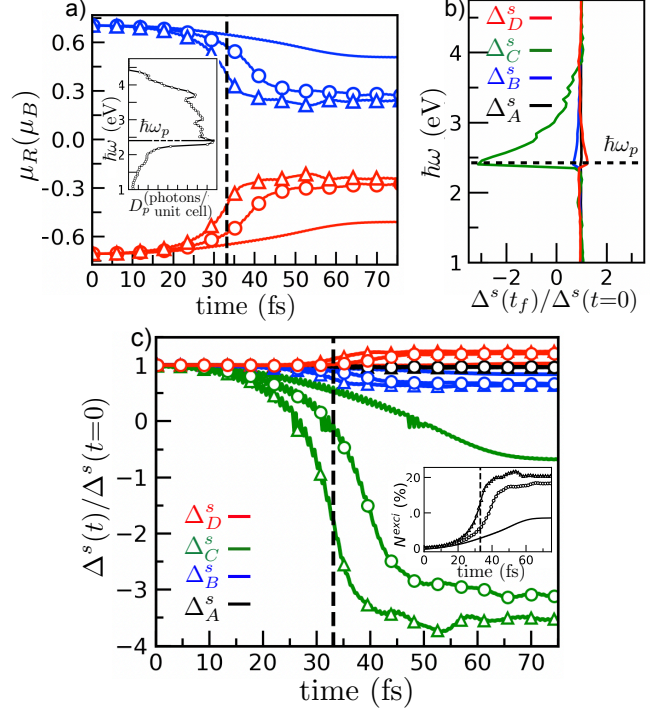


FIG. 3. (a) Evolution of the local magnetic moment of the spin-up (blue) and spin-down (red) TM-sites during and after light-pulse with photon energy $\hbar\omega_p = 2.39$ eV for different N^{exci} . The inset shows the photon absorption density D_p versus the excitation energy $\hbar\omega$, where the horizontal line indicates $\hbar\omega_p = 2.39$. (b) Relative change in spin-splitting $\Delta^s(t_o)/\Delta^s(t=0)$ at the high-symmetry point X at $t_f=50$ fs. (c) Evolution of percentage of excited electrons (inset) and $\Delta^s(t)/\Delta^s(t=0)$ (main) at X-point after photoexcitation for various light intensities. Lines with triangles, circles, and without symbols correspond to $N^{exci} = 8.50\%$, 18.30% and 20.30% , respectively, after $t_f=50$ fs in both figures b and c. The vertical line marks the zero point of the 30-fs Gaussian light pulse. The model parameters are consistent with the panel (e) in Figure 1.

$$\sum_{q=1}^{N_e} |\langle \psi_q(\vec{k}, t) | \phi_m(\vec{k}, t) \rangle|^2.$$

The ratio of photo-excited electrons is

$$N^{exci} = \frac{1}{2} \frac{\sum_{\vec{k}} |f_m(\vec{k}, t_f) - f_m(\vec{k}, t_i)|}{\sum_{\vec{k}} f_m(\vec{k}, t_i)} \quad (12)$$

where t_i is a time before and t_f is a time after the light pulse. The spin-splitting gaps $\Delta^s(t)$ are extracted from the eigenvalues $\epsilon_n(\vec{k}, t)$ of the instantaneous electronic Hamiltonian. The z-component of the local magnetic moment for site R is

$$\mu_{z,R}(t) = \sum_{\alpha,n} \left(\left| \psi_{\uparrow,\alpha,R,n}(t) \right|^2 - \left| \psi_{\downarrow,\alpha,R,n}(t) \right|^2 \right). \quad (13)$$

Figures 3-a and 3-c show the evolution of local magnetic moments μ_R and spin-splittings relative spin-splitting $\Delta^s(t)/\Delta^s(t=0)$ for light pulses with three different intensities, corresponding to $N^{exci} = 8.50\%$, 18.30% ,

and 20.30% photoexcited electrons. The optical excitations are charge-transfer transitions between neighboring TM-sites. Because the two sites participating in the charge transfer are antiferromagnetic, the excitation reduces their magnetic moments, which is evident in Figure 3-a (blue and red).

The spin-splitting gaps respond instantaneously, i.e. during the photoexcitation process: Two of the spin-splitting gaps, namely Δ_B^s and Δ_C^s respond strongly to optical excitation. For $N^{exci} = 18.30\%$ we find a change of 0.35 eV of Δ_B^s and 0.41 eV of Δ_C^s . The other spin-splittings are small in comparison with a change of 0.01 eV in Δ_A^s and 0.08 eV in Δ_D^s .

The spin-splitting gap with the largest response to photoexcitation, namely Δ_C^s , is between states that were nearly degenerate initially. This spin-splitting gap, Δ_C^s , is in the upper conduction band, where most of the excited electrons are located. Initially, the spin-splitting Δ_C^s falls off to zero, and then rises again with an opposite sign. For the more intense excitations, i.e. with $N^{exci} = 18.30\%$ and 20.30%, $\Delta_C^s(t)$ becomes nearly four times its equilibrium value within 50 fs, see Figure 3-c (green).

Figure 3-b shows the relative change in spin-splitting $\Delta^s(t_f)/\Delta^s(t=0)$ at the high-symmetry point X at $t_f=50$ fs as a function of photon energy $\hbar\omega$. The largest changes $\Delta^s(t_f)/\Delta^s(t=0)$ of the spin-splitting gaps occur for photon energies near the bottom of the broad absorption peak, namely at $\hbar\omega_p=2.39$ eV.

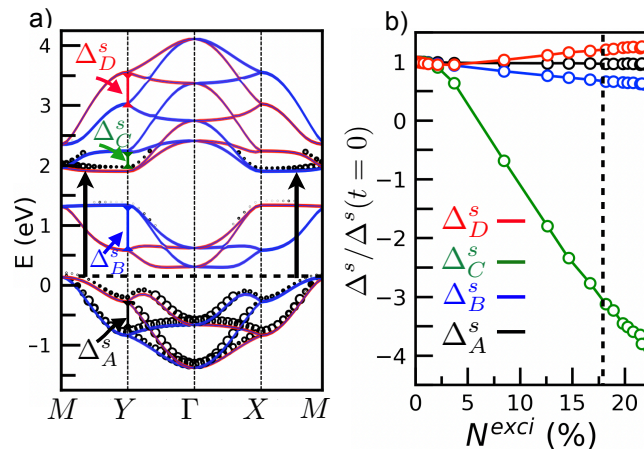


FIG. 4. (a) Band structure of the photoexcited altermagnet at $\hbar\omega_p = 2.39$ eV and $N^{exci}=18.30\%$, showing also the electron distribution in the valence and conduction bands. The size of the circles represents the occupancy of the electronic levels. The horizontal dashed line indicates the Fermi level. The vertical arrows indicate the electronic transitions. (b) Spin-splitting gaps as a function of the percentage N^{exci} (%) of photoexcited electrons with $\hbar\omega_p = 2.39$ eV. The vertical line indicates $N^{exci}=18.30\%$.

Let us rationalize the findings described above on the level of local orbitals. For the sake of the argument, we consider here only the diagonal elements of the one-

particle reduced density matrix. The photo excitation with photon energy at the absorption maximum transfers electrons from the lower, majority spin orbital of one site to the upper, minority spin orbital of a neighboring site. This implies that, on each site, the occupation change $\delta n_{l,\downarrow,R}$ of the filled orbital equals $-N^{exci}$, while the occupation $\delta n_{u,\uparrow,R}$ of the upper, minority-spin orbital changes by $+N^{exci}$. Figure 4-a shows the electron distribution in the photo-excited state at time $t=75$ fs for $N^{exci} = 20.30\%$. The excited electrons predominantly occupy the upper conduction band on the $X - M$ and the $Y - M$ high-symmetry lines in reciprocal space.

The orbital energies are obtained using Janak's theorem[17], as the derivative of total energy with respect to occupations $n_{\sigma\alpha}$ (see SI for more information). Hence, the occupation changes $\delta n_{\alpha,\sigma,R}$ result in a response $\delta \bar{\epsilon}_{\beta,\sigma',R}$ of the orbital energies of the form $\delta \bar{\epsilon}_{\alpha,\sigma,R} = \sum_{\beta,\sigma'} \frac{\partial^2 E_{coul}}{\partial n_{\alpha,\sigma,R} \partial n_{\beta,\sigma',R}} \delta n_{\beta,\sigma',R}$.

It turns out that the same orbitals, which experience the largest occupation changes, experience also the largest energy level shifts, namely $\delta \bar{\epsilon}_{l,\downarrow,R} = -\delta \bar{\epsilon}_{u,\uparrow,R} = (U - 2J)N^{exci}$. The band structure changes according to the k-dependent orbital weights, i.e. $\delta \epsilon_n(\vec{k}) = \sum_{\alpha,\sigma,R} |\langle \psi_n(\vec{k}) | \Theta_{\alpha,\sigma,R} \rangle|^2 \delta \bar{\epsilon}_{\alpha,\sigma,R}$.

Let us investigate the changes in the spin-splitting gaps as a function of the photoexcited electron population N^{exci} . The most significant changes in relative spin-splitting with increasing N^{exci} are observed for Δ_C^s , see Figure 4-b. Remarkably, Δ_C^s increases up to four times its initial value at high N^{exci} .

Our study demonstrates that spin-splittings of altermagnets can be modified and controlled by optical excitations. These changes occur on ultrafast time scales. Promising candidates to realize this effect are 3d transition-metal compounds. The temporal change in spin-splittings predicted here can experimentally be probed by time-resolved spin angle-resolved photoemission spectroscopy (SARPES) [18–20].

In conclusion, we demonstrate that optical excitations significantly modify the spin-splitting gaps in an altermagnet with correlated electrons. We study this effect by employing real-time simulations based on an interacting tight-binding model. The modification in spin-splitting is driven by the photoinduced changes in the band structure. The magnitude of changes in spin-splittings is strongly sensitive to the intensity of the light-field. Our findings suggest that light fields can be an effective tool for modifying the altermagnetic properties of strongly correlated systems on ultrafast timescales.

Acknowledgments: Theory and simulation were supported by the Computational Materials Sciences (CMS) Program funded by the US Department of Energy, Office of Science, Basic Energy Sciences, Materials Sciences and Engineering Division. Data analysis was provided by the User Program of the Molecular Foundry, supported by the Office of Science, Office of Basic Energy Sciences, of the U.S. Department of Energy under Con-

tract No. DE-AC02-05CH11231. This work was performed under the auspices of the U.S. Department of Energy by Lawrence Livermore National Laboratory under Contract DE-AC52-07NA27344. This work was performed under the auspices of the U.S. Department of Energy by Lawrence Livermore National Laboratory under Contract DE-AC52-07NA27344. S.R. and T.O. are

supported by the Computational Materials Sciences Program funded by the US Department of Energy, Office of Science, Basic Energy Sciences, Materials Sciences and Engineering Division. This work is funded in parts by the Deutsche Forschungsgemeinschaft (DFG, German Research Foundation) 217133147/SFB1073, projects B03 and C03.

-
- [1] L. Šmejkal, J. Sinova, and T. Jungwirth, *Phys. Rev. X* **12**, 040501 (2022).
- [2] L. Šmejkal, R. González-Hernández, T. Jungwirth, and J. Sinova, *Science Advances* **6**, eaaz8809 (2020), <https://www.science.org/doi/pdf/10.1126/sciadv.aaz8809>.
- [3] L. Šmejkal, J. Sinova, and T. Jungwirth, *Phys. Rev. X* **12**, 031042 (2022).
- [4] Z. Feng, X. Zhou, L. Šmejkal, L. Wu, Z. Zhu, H. Guo, R. González-Hernández, X. Wang, H. Yan, P. Qin, X. Zhang, H. Wu, H. Chen, Z. Meng, L. Liu, Z. Xia, J. Sinova, T. Jungwirth, and Z. Liu, *Nature Electronics* **5**, 735 (2022).
- [5] R. D. Gonzalez Betancourt, J. Zubáč, R. Gonzalez-Hernandez, K. Geishendorf, Z. Šobáň, G. Springholz, K. Olejník, L. Šmejkal, J. Sinova, T. Jungwirth, S. T. B. Goennenwein, A. Thomas, H. Reichlová, J. Železný, and D. Kriegner, *Phys. Rev. Lett.* **130**, 036702 (2023).
- [6] I. Gray, Q. Deng, Q. Tian, M. Chilcote, M. Brahlek, and L. Wu, *arXiv e-prints*, [arXiv:2404.05020](https://arxiv.org/abs/2404.05020) (2024), [arXiv:2404.05020 \[cond-mat.mtrl-sci\]](https://arxiv.org/abs/2404.05020).
- [7] Y. Guo, H. Liu, O. Janson, I. Cosma Fulga, J. van den Brink, and J. I. Facio, *Materials Today Physics* **32**, 991 (2023), [arXiv:2207.07592 \[cond-mat.mtrl-sci\]](https://arxiv.org/abs/2207.07592).
- [8] A. de la Torre, D. M. Kennes, M. Claassen, S. Gerber, J. W. McIver, and M. A. Sentef, *Rev. Mod. Phys.* **93**, 041002 (2021).
- [9] S. Rajpurohit, J. Simoni, and L. Z. Tan, *Nanoscale Adv.* **4**, 4997 (2022).
- [10] S. Rajpurohit, C. Jooss, and P. E. Blöchl, *Phys. Rev. B* **102**, 014302 (2020).
- [11] M. Sotoudeh, S. Rajpurohit, P. Blöchl, D. Mierwaldt, J. Norpoth, V. Roddatis, S. Mildner, B. Kressdorf, B. Iffland, and C. Jooss, *Phys. Rev. B* **95**, 235150 (2017).
- [12] S. Yunoki, T. Hotta, and E. Dagotto, *Phys. Rev. Lett.* **84**, 3714 (2000).
- [13] C. Şen, G. Alvarez, and E. Dagotto, *Phys. Rev. Lett.* **105**, 097203 (2010).
- [14] S. Rajpurohit, L. Z. Tan, C. Jooss, and P. E. Blöchl, *Phys. Rev. B* **102**, 174430 (2020).
- [15] E. Runge and E. K. U. Gross, *Phys. Rev. Lett.* **52**, 997 (1984).
- [16] R. Peierls, *Zeitschrift für Physik* **80**, 763 (1933).
- [17] J. F. Janak, *Phys. Rev. B* **18**, 7165 (1978).
- [18] F. Boschini, M. Zonno, and A. Damascelli, *Rev. Mod. Phys.* **96**, 015003 (2024).
- [19] J. A. Sobota, Y. He, and Z.-X. Shen, *Rev. Mod. Phys.* **93**, 025006 (2021).
- [20] T. Rohwer, S. Hellmann, M. Wiesenmayer, C. Sohr, A. Stange, B. Slomski, A. Carr, Y. Liu, L. M. Avila, M. Kalläne, S. Mathias, L. Kipp, K. Rossnagel, and M. Bauer, *Nature* **471**, 490 (2011).